Small Coronal Holes Near Active Regions as Sources of Slow Solar Wind

Y.-M. Wang
Space Science Division, Naval Research Laboratory, Washington, DC 20375, USA; yi.wang@nrl.navy.mil

Abstract

We discuss the nature of the small areas of rapidly diverging, open magnetic flux that form in the strong unipolar fields at the peripheries of active regions (ARs), according to coronal extrapolations of photospheric field measurements. Because such regions usually have dark counterparts in extreme-ultraviolet (EUV) images, we refer to them as coronal holes, even when they appear as narrow lanes or contain sunspots. Revisiting previously identified "AR sources" of slow solar wind from 1998 and 1999, we find that they are all associated with EUV coronal holes; the absence of well-defined He I 1083.0 nm counterparts to some of these holes is attributed to the large flux of photoionizing radiation from neighboring AR loops. Examining a number of AR-associated EUV holes during the 2014 activity maximum, we confirm that they are characterized by wind speeds of $\sim$300–450 km s^{-1}, O^{7+}/O^{6+} ratios of $\sim$0.05–0.4, and footpoint field strengths typically of order 30 G. The close spacing between ARs at sunspot maximum limits the widths of unipolar regions and their embedded holes, while the continual emergence of new flux leads to rapid changes in the hole boundaries. Because of the highly nonradial nature of AR fields, the smaller EUV holes are often masked by the overlying canopy of loops, and may be more visible toward one solar limb than at central meridian. As sunspot activity declines, the AR remnants merge to form much larger, weaker, and longer-lived unipolar regions, which harbor the "classical" coronal holes that produce recurrent high-speed streams.

Key words: solar wind – Sun: activity – Sun: corona – Sun: heliosphere – Sun: magnetic fields – Sun: UV radiation

1. Introduction

Because of its distinctive compositional properties and high spatial/temporal variability, low-speed ($\lesssim$450 km s^{-1}) solar wind is widely assumed to come from outside coronal holes, which are generally agreed to be the source of high-speed streams (see the review of Abbo et al. 2016). A prevalent idea is that the slow wind is continually released from closed coronal loops, which transfer their contents to nearby open field lines by "interchange" reconnection; the loop material is characterized by relatively high charge-state ratios and by enrichment in elements of low first-ionization potential, consistent with in situ measurements of slow wind (see, e.g., Schwadron et al. 1999; Zurbuchen et al. 2000). Indeed, white-light observations of outward-propagating density inhomogeneities (small flux ropes or "blobs") and of ray-like fine structure provide evidence that the slow wind in the immediate vicinity of the heliospheric current/plasma sheet originates from coronal streamers (Wang et al. 2000; Sheeley et al. 2009). However, in order to account for the presence of low wind speeds far from interplanetary sector boundaries, the interchange reconnection scenario seems to require a large-scale mixing of closed and open flux that is not confined to the edges of coronal holes.

An alternative view is that, like the fast wind, the bulk of the slow wind originates from open-field regions, with its compositional properties depending on parameters such as the footpoint field strength and the rate at which the open flux diverges with height. This hypothesis is supported by the inverse correlation between observed wind speed and coronal flux-tube expansion, as inferred from extrapolations of the photospheric field (see, e.g., Levine et al. 1977; Wang & Sheeley 1990; Arge & Pizzo 2000; Cohen 2015; Poduval 2016). On physical grounds, if the heating rate depends on the local coronal field strength, the effect of rapid

flux-tube divergence is to concentrate the heating near the coronal base, increasing the mass flux but decreasing the energy available to accelerate the wind (Wang & Sheeley 2003; Cranmer et al. 2007; Wang et al. 2009).

If open-field regions are taken to be the same as coronal holes, a prediction of the expansion factor model is that most of the slow wind should come from small coronal holes and from just inside the boundaries of both large and small holes. However, the relationship between open-field regions and coronal holes has long been regarded as ambiguous (see, e.g., Levine 1982). On the one hand, the locations of open flux derived from photospheric field extrapolations are subject to considerable uncertainties, both because of deficiencies in the magnetograms (including zero-point calibration errors and noisy polar-field measurements) and because of the oversimplified nature of the coronal models (even those that include current sheets and other magnetohydrodynamic effects). On the other hand, there is no general agreement as to what constitutes a coronal hole; their locations often depend on which particular wavelength is used to identify them. An important question concerns the nature of the observational counterparts to the small areas of open flux that are predicted to occur in and around active regions (ARs; see, e.g., Švestka et al. 1977; Levine 1982; Liewer et al. 2003, 2004; Schrijver & DeRosa 2003; Wang et al. 2010; Brooks et al. 2015; Fu et al. 2015, 2017; Fazakerley et al. 2016).

The objective of this study is to clarify the relationship between the predicted open flux near ARs, small coronal holes, and the slow wind that dominates the heliosphere around sunspot maximum. After outlining our basic procedure (Section 2), we re-examine a number of cases from the previous solar cycle and address the question of why open-field regions next to ARs often appear to have counterparts in the extreme ultraviolet (EUV) but not in He I 1083.0 nm (Section 3). In Section 4, we use EUV images from the *Solar Dynamics Observatory* (*SDO*) and in situ measurements to

CR 1934 (1998 MARCH 18 - APRIL 14)
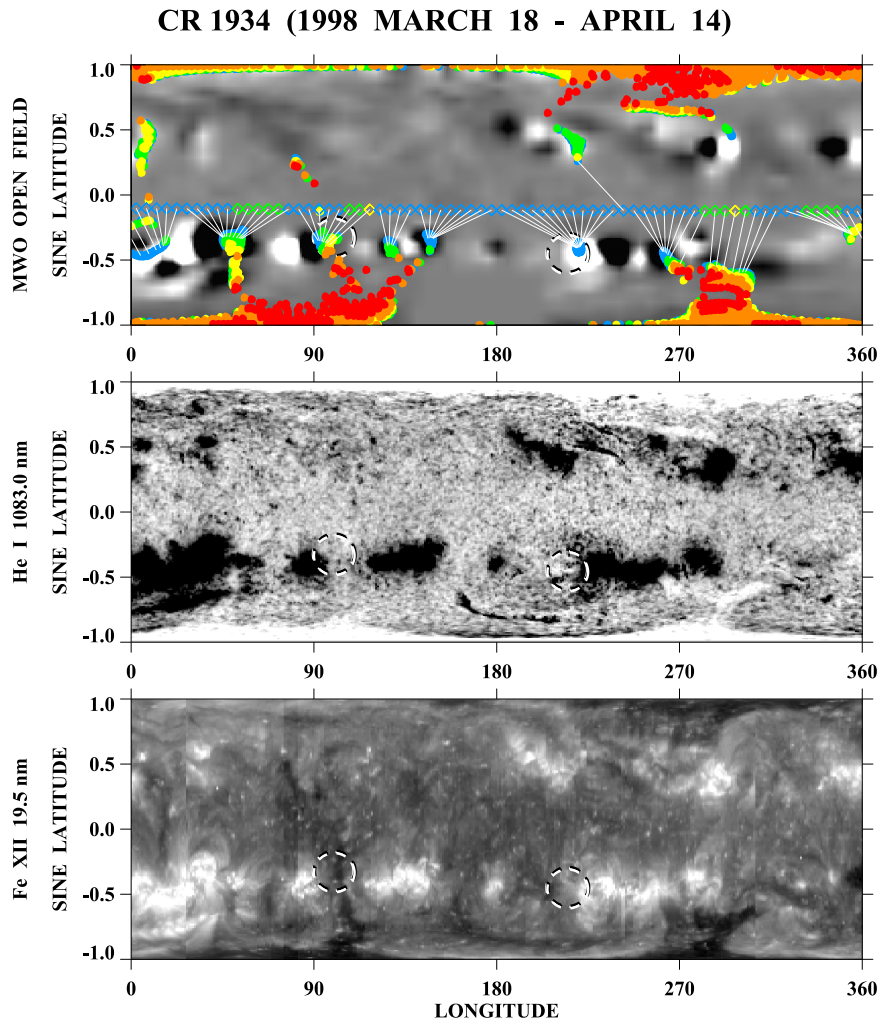
Figure 1. Carrington-format maps showing the predicted and observed configuration of coronal holes during CR 1934. Top panel: MWO photospheric field, with PFSS-derived open-field regions overplotted as colored dots. Grayscale contours for the photospheric field range from black ($B_r < -20$ G) to white ($B_r > +20$ G). Footpoint areas of open flux are color-coded to indicate the associated flux-tube expansion factors: blue ($f_{ss} > 35$), green ($15 < f_{ss} < 35$), yellow ($8 < f_{ss} < 15$), orange ($4 < f_{ss} < 8$), and red ($f_{ss} < 4$). Colored diamonds (plotted in the ecliptic plane) indicate the expansion factors of Earth-directed flux tubes, with white lines connecting them to their footpoints. Middle panel: NSO map of He I 1083.0 nm intensity. In general, white (black) areas represent coronal holes or filament channels (ARs or filaments). Bottom panel: distribution of Fe XII 19.5 nm emission recorded by EIT. Circled areas at longitudes ∼100° and ∼215° highlight features discussed in the text.

identify some of the sources of slow wind during the 2014 sunspot maximum, and discuss the nature of the source regions. Our conclusions are summarized in Section 5.

2. Procedure

As in most previous studies (e.g., Levine 1982; Wang et al. 1996, 2010; Luhmann et al. 2002; Liewer et al. 2003, 2004; Schrijver & DeRosa 2003; Ko et al. 2014; Brooks et al. 2015; Fu et al. 2015, 2017; Fazakerley et al. 2016; Fujiki et al. 2016), we determine the locations of open flux by applying a potential-field source-surface (PFSS) extrapolation to photospheric field measurements. As demonstrated by Neugebauer et al. (1998) and Riley et al. (2006), the PFSS-derived open-field regions are generally in good agreement with MHD calculations.

Let r denote heliocentric distance, L heliographic latitude, and ϕ Carrington longitude. In our version of the PFSS model, the magnetic field $\boldsymbol{B}(r, L, \phi)$ remains current-free from the coronal base to $r = R_{ss} = 2.5\ R_\odot$, where B_L and B_ϕ are required to

vanish; all field lines that cross the source surface are considered to be "open." At $r = R_\odot$, B_r is matched to the photospheric field, assumed to be approximately radial at the depth where it is measured (see Wang & Sheeley 1992). The magnetograph data employed here are in the form of 27.3 day synoptic maps from the National Solar Observatory (NSO), the Mount Wilson Observatory (MWO; available until the end of 2012), and the Wilcox Solar Observatory (WSO). The MWO and WSO measurements are corrected for the saturation of the Fe I 525.0 nm line profile by multiplying them by a latitude-dependent factor (4.5–$2.5 \sin^2 L$; Wang & Sheeley 1995). Comparison of the results obtained from the three observatories gives an indication of the uncertainties involved in the predicted locations of open flux (as illustrated in the next section). Because we interpolate the photospheric field maps to a resolution of 5° in latitude and longitude (which is of the same order as the expected accuracy of our extrapolations), we are unable to reproduce any of the supergranular-scale fine structure seen in the EUV and helium images of coronal holes.

CR 1934 - COMPARISON OF MWO, NSO, & WSO
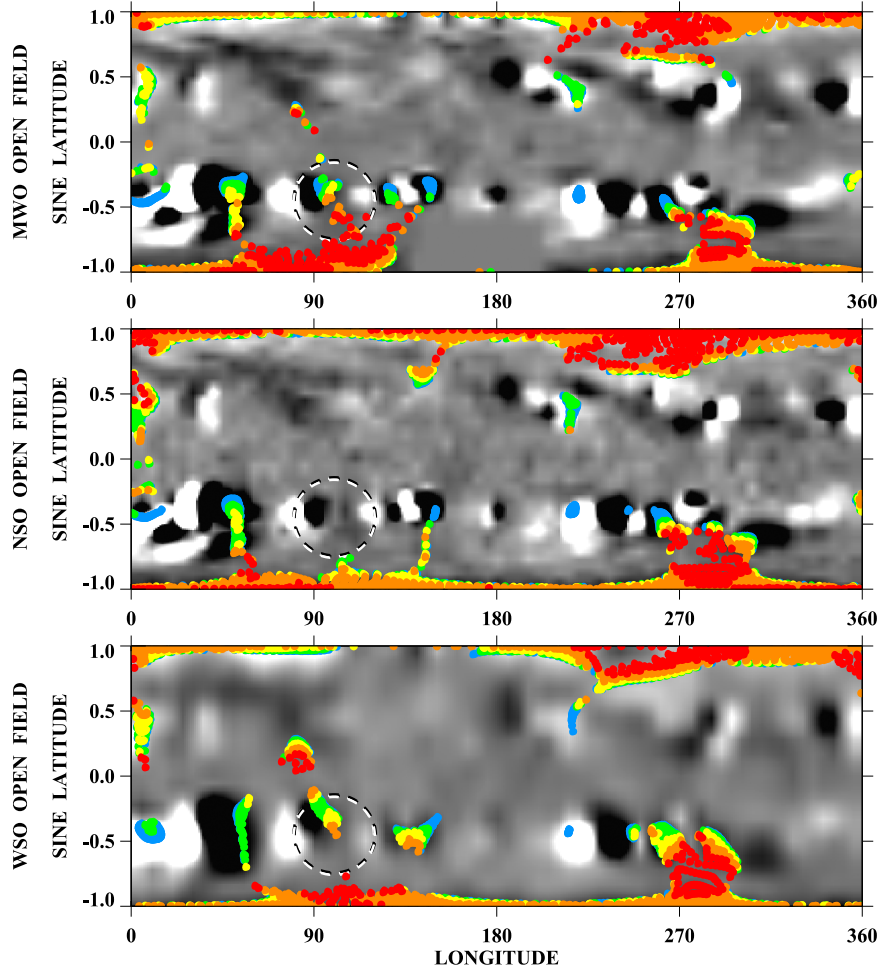
Figure 2. Open-field regions derived for CR 1934 using magnetograph measurements from MWO (top panel), NSO (middle panel), and WSO (bottom panel). The footpoint areas of open flux, color-coded as in Figure 1, are overplotted on the photospheric field, which is here saturated at $B_r = \pm 10$ G. The three observatories yield differing results in the circled area, where the EUV map of Figure 1 shows an equatorward extension of the south polar hole.

The factor by which an open flux tube expands in solid angle between the coronal base and the source surface is calculated as

$$f_{\mathrm{ss}} = \left(\frac{R_{\odot}}{R_{\mathrm{ss}}}\right)^2 \frac{B_0}{|B_{\mathrm{ss}}|}, \qquad (1)$$

where B_0 and $|B_{\mathrm{ss}}|$ denote the footpoint and source-surface field strengths, respectively.

To identify the observational counterparts of open-field regions, we use EUV data from the EUV Imaging Telescope (EIT) on the *Solar and Heliospheric Observatory* (*SOHO*) and from the Atmospheric Imaging Assembly (AIA) on *SDO*. These images are supplemented by line-of-sight magnetograms from the Michelson Doppler Interferometer (MDI) and the Helioseismic and Magnetic Imager (HMI). In Section 3, we also make use of He I 1083.0 nm observations from the NSO/Kitt Peak Vacuum Telescope.[1]

Solar wind speed and interplanetary magnetic field (IMF) measurements during early 2014 are extracted as hourly averages from the OMNIWeb site,[2] and two-hourly averages

of O^{7+}/O^{6+} are obtained from the *Advanced Composition Explorer* (*ACE*) SWICS 2.0 database.[3] For consistency with the spatial/temporal resolution of our coronal extrapolations, the data are smoothed by taking 10 hr running averages. The source locations of the near-Earth wind are found by tracing inward along the magnetic field, taking into account the longitude shift due to solar rotation.

## 3. Case Studies of AR-associated Coronal Holes During 1998–1999

In an isolated AR, regarded as a large bipolar magnetic region (BMR), the coronal loops that connect the opposite ends of the BMR extend to great heights and are dragged outward to become part of the solar wind. A pair of opposite-polarity coronal holes is thus expected to form at the far ends of the AR. If the AR is located near other ARs or their remnants, holes will tend to form where the polarity of the AR field matches that of the background field. The open flux rooted in these unipolar areas then divides the internal AR loop system from the neighboring ones (see, e.g., Švestka et al. 1977). Open flux

---
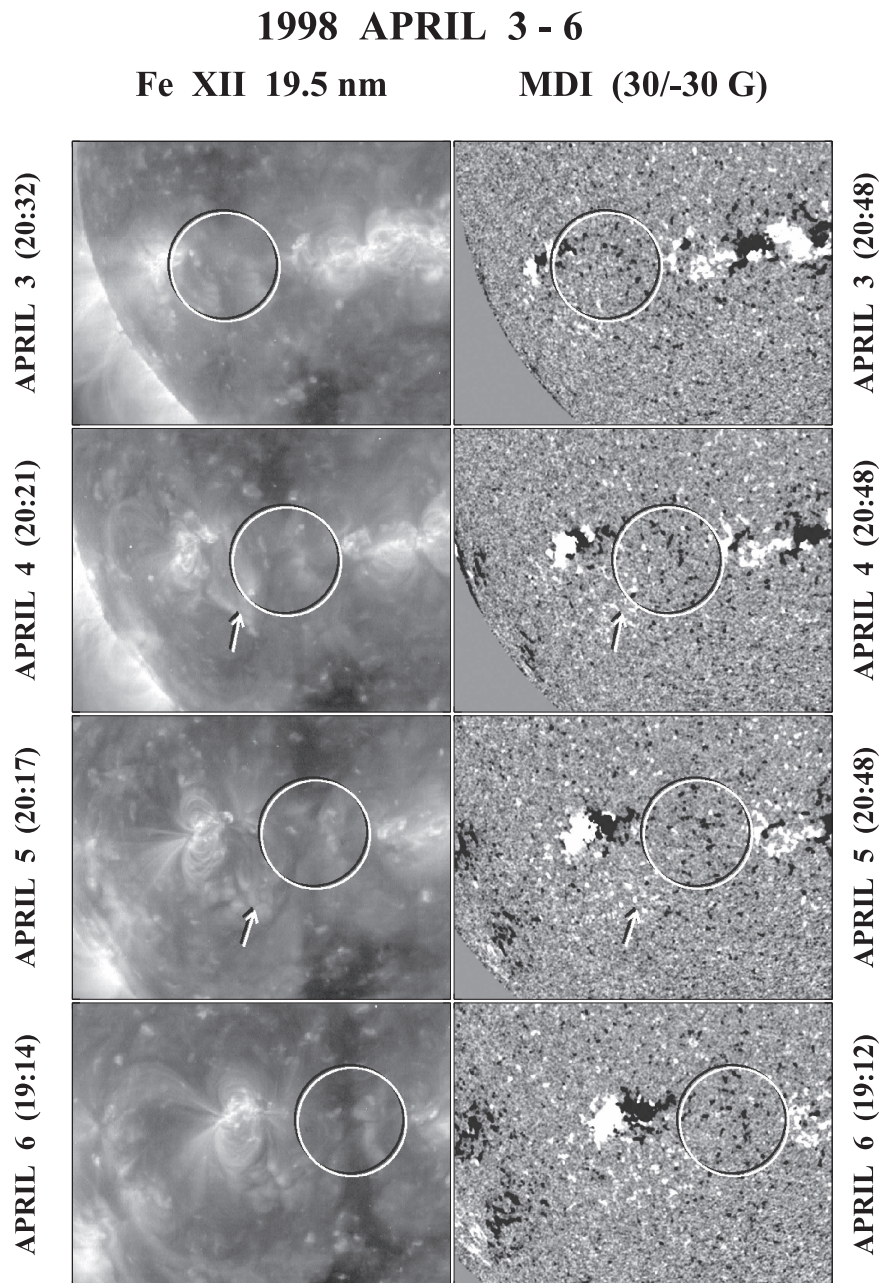
Figure 3. Sequence of EIT Fe XII 19.5 nm images (left column) and MDI magnetograms (right column) recorded during 1998 April 3–6, showing the growth of NOAA AR 8193 and the formation of the polar hole extension located at $\phi \sim 100°$ in Figure 1. In the magnetograms, the line-of-sight field has been saturated at ± 30 G. Circled areas have radius 148″. Arrows point to connections formed between the negative-polarity sector of the new AR and the positive-polarity background field to its southwest. The polar hole extension forms inside the negative-polarity corridor between the AR and the activity complex to its west.

may also be transferred to the outskirts of an AR by interchange reconnection between the high AR loops and background coronal holes (as illustrated in Figure 1 of Wang & Sheeley 2004).

As noted by Levine (1982), the small, AR-associated areas of open flux predicted by the coronal extrapolation models usually have corresponding dark features in EUV and soft X-ray images, but are often unidentifiable in He I 1083.0 nm spectroheliograms. For that reason, and because they are much smaller than the prototype coronal holes that produced the recurrent high-speed streams of the *Skylab* era, such regions have generally not been labeled as coronal holes.

Instead, Neugebauer et al. (2002) and Liewer et al. (2003, 2004) referred to them as "AR sources" of solar wind, with the implication that they differ fundamentally from coronal holes. However, we will here use the term "coronal hole" to refer to any dark EUV feature that lies inside a unipolar area and that is located near (within ~5° of) a predicted open-field region. (A "unipolar" area is defined as being dominated by a single polarity on large scales, but not necessarily on sub-supergranular scales; it may include flux located inside or outside ARs.)

Liewer et al. (2003, 2004) described several cases of AR sources of near-Earth wind during 1998–1999, in which the

CR 1953 (1999 AUGUST 18 - SEPTEMBER 14)
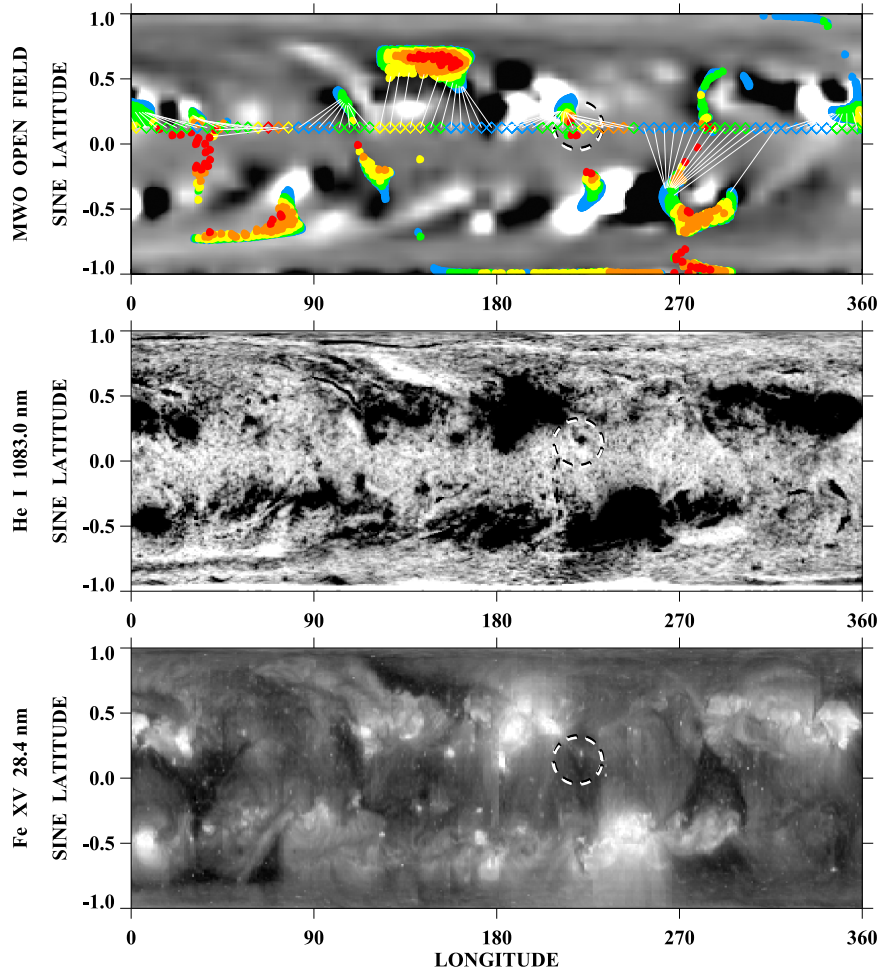
Figure 4. Carrington-format maps showing the predicted and observed configuration of coronal holes during CR 1953. Top panel: MWO photospheric field, with PFSS-derived open-field regions overplotted as colored dots. Grayscale contours and color-coding as in Figure 1. Middle panel: NSO map of He I 1083.0 nm intensity. Bottom panel: distribution of Fe XV 28.4 nm emission recorded by EIT. Circled area at $\phi \sim 220°$ contains a coronal hole discussed in the text (see also Figure 5).

corresponding open-field regions apparently had neither He I 1083.0 nm nor spatially coincident EUV/X-ray counterparts. It is instructive to revisit these examples, which provide informative case studies of open flux in and around ARs.

3.1. Nature of the Solar-wind Source Regions Near ARs 8185 and 8193

Figure 1 displays, as a function of latitude and longitude for Carrington rotation (CR) 1934 (1998 March 18–April 14), the MWO photospheric field with the PFSS-derived open-field regions overplotted, the distribution of He I 1083.0 nm intensity from NSO, and the distribution of Fe XII 19.5 nm emission from EIT. The open-field areas are color-coded to represent the rate of flux-tube divergence, with the largest (smallest) values of f_{ss} denoted by blue (red) dots. Colored diamonds indicate the expansion factors of Earth-directed flux tubes, with white lines connecting their ecliptic positions to their photospheric footpoints. The circles enclose two AR sources of solar wind identified by Liewer et al. (2003); the wind speeds V recorded at ACE were in the range ~300–400 km s^{-1}.

The small open-field region at longitude $\phi \sim 215°$ has a clearly defined He I 1083.0 nm counterpart (which, however, does not appear on the hand-drawn synoptic map of hole boundaries provided by NSO). In this particular case, the coronal hole is more clearly seen in the 1083.0 nm line than in the Fe XII 19.5 nm line (bottom panel of Figure 1), where it is partially hidden beneath the bright loops fanning out eastward from NOAA AR 8185. When the hole is tracked in individual EIT 19.5 and 28.4 nm images, however, its western edge becomes visible as the AR rotates toward the west limb and the overlying loops are no longer oriented transverse to the line of sight.

The circle near longitude $100°$ contains a dark area in Fe XII which approximately coincides with the open-field footpoints predicted from the MWO photospheric field, and which is part of an equatorward extension of the south polar hole. In the NSO-based extrapolation of Liewer et al. (2003), the open flux is rooted just eastward of the observed dark lane, closer to the core of AR 8193. The absence of a corresponding feature in the He I 1083.0 nm map could be due to the fact that no observations were made at NSO on April 6, when the equatorward extension crossed central
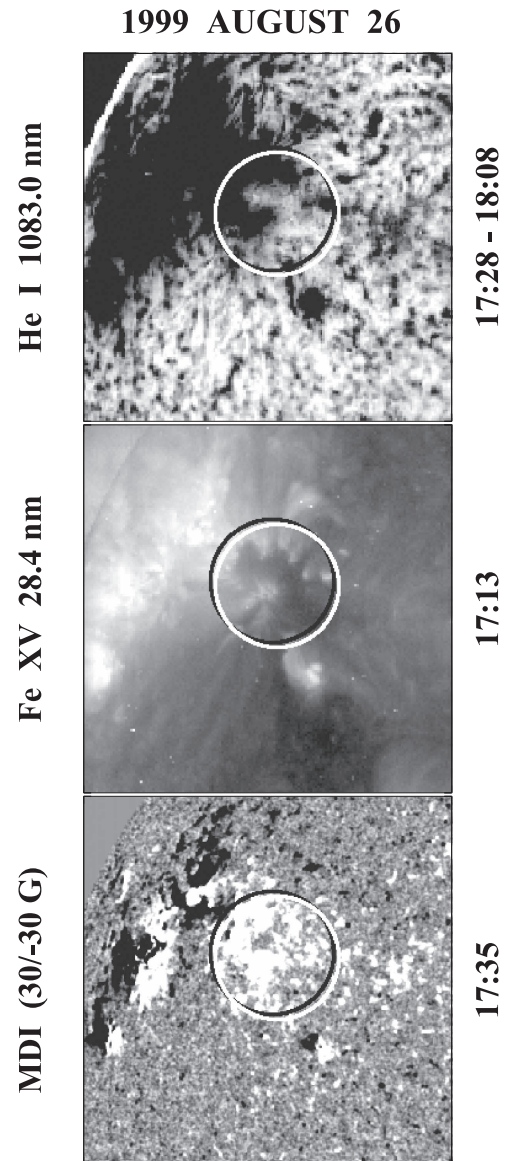
5
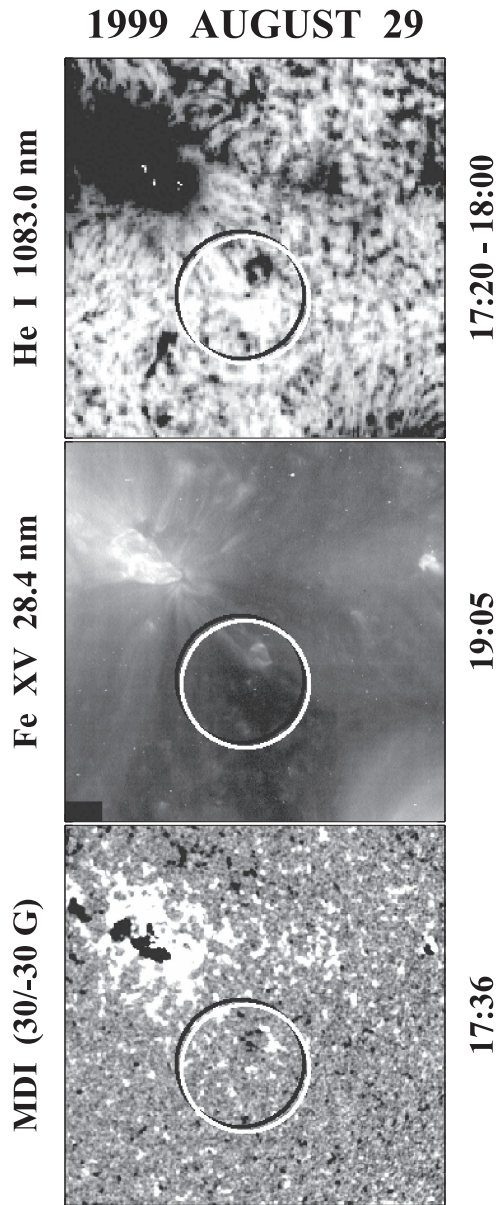
1999 AUGUST 29

Figure 5. Close-up view of the coronal hole seen at longitude ∼220° in the synoptic maps of Figure 4. Top panel: He I 1083.0 nm image taken at NSO/Kitt Peak around 17:40 UTC on 1999 August 29. Middle panel: Fe XV 28.4 nm image recorded by EIT at 19:05 UTC. Bottom panel: MDI magnetogram recorded at 17:36 UTC; the line-of-sight field has been saturated at ±30 G. AR 8681 lies to the northeast of the circled area, which has radius 130″.

1999 AUGUST 26

Figure 6. Extension of the low-latitude coronal hole of Figure 5 into the positive-polarity plage region to the northeast, as seen on 1999 August 26, prior to the emergence of AR 8681. Top panel: He I 1083.0 nm image taken around 17:48 UTC. Middle panel: Fe XV 28.4 nm image recorded at 17:13 UTC. Bottom panel: MDI magnetogram recorded at 17:35 UTC and saturated at ±30 G. Circled area has radius 130″. The 1083.0 nm counterpart of the EUV hole tends to be darker where bright loops are rooted next to the hole boundaries.

meridian (a whitish area is present on the spectroheliogram recorded on April 7).

Figure 2 compares the open-field regions that we derived for CR 1934 using photospheric field measurements from MWO, NSO, and WSO. The equatorward extension of the south polar hole seen in the EUV map of Figure 1 is entirely missing from the PFSS extrapolation of the NSO map (middle panel of Figure 2). The WSO-based extrapolation (bottom panel) shows only the low-latitude part of the extension; we also remark that the positive-polarity sector of AR 8193 seems to be shifted too far poleward in the photospheric field map.

As shown by the sequence of EIT 19.5 nm images and MDI magnetograms in Figure 3, the polar hole extension

formed early on April 6, a few days after the emergence of AR 8193 near the east limb at latitude $L \sim -22°$. As the AR grew, its negative-polarity sector became linked to the positive-polarity background field to the southwest (as suggested by the arrowed 19.5 nm structures in Figure 3); subsequently, some of the negative-polarity background flux located to the west evidently opened up. An ejection that occurred in the activity complex westward of AR 8193 during April 4–5 may also have served as a trigger or catalyst for the formation of the dark channel. The sudden appearance of this structure, as well as the absence of a corresponding open-field region in our NSO extrapolation, suggests that it should be classified as a transient or "marginally stable"

1999 AUGUST 27 - 29

Fe IX 17.1 nm   MDI (300/-300 G)
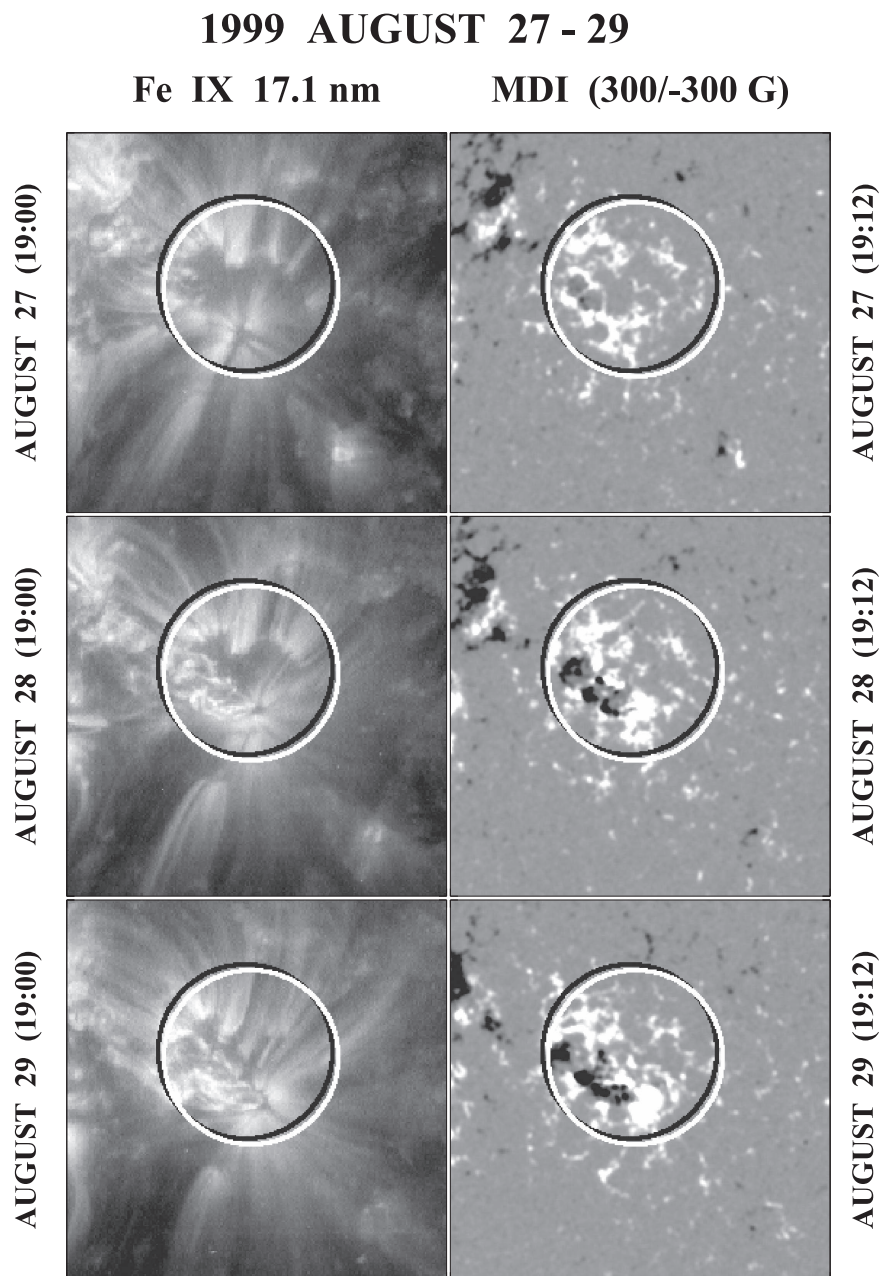
Figure 7. Closing-down of the small coronal hole of Figure 6 during the emergence of AR 8681, 1999 August 27–29. Left panels: sequence of EIT Fe IX 17.1 nm images, showing the evolution of loop structures in and around the hole. Right panels: corresponding MDI magnetograms saturated at ±300 G. Circles have radius 119″.

coronal hole; small perturbations in the ambient coronal field may have caused the flux inside the narrow negative-polarity corridor to open up.

3.2. The Case of AR 8681

AR 8681, located at $L \sim +21°$, emerged near central meridian during 1999 August 27–29. Figure 4 displays the MWO photospheric field and PFSS-derived open-field regions for CR 1953, together with the corresponding He I 1083.0 nm and Fe XV 28.4 nm maps. The circle encloses an area of open flux that extends equatorward from the edge of AR 8681, which is situated at the western end of the bright activity

complex seen in the 28.4 nm map. The predicted open-field footpoints coincide approximately with a white patch in the helium map and a dark region in Fe XV, confirming that the open flux is rooted in a coronal hole.

Figure 5 provides a close-up view of the coronal hole and its immediate surroundings on August 29, as seen in individual 1083.0 and 28.4 nm images and an MDI magnetogram. The hole lies within a background unipolar region located to the southwest of the newly emerged AR. The PFSS extrapolation (top panel of Figure 4) predicts that this positive-polarity hole was connected to the ecliptic plane, with the Earth-directed flux tubes having a wide range of expansion factors (from $f_{ss} > 35$ to $f_{ss} < 8$). In situ measurements by *ACE* (not plotted here, but

CR 1957 (1999 DECEMBER 5 - 2000 JANUARY 1)
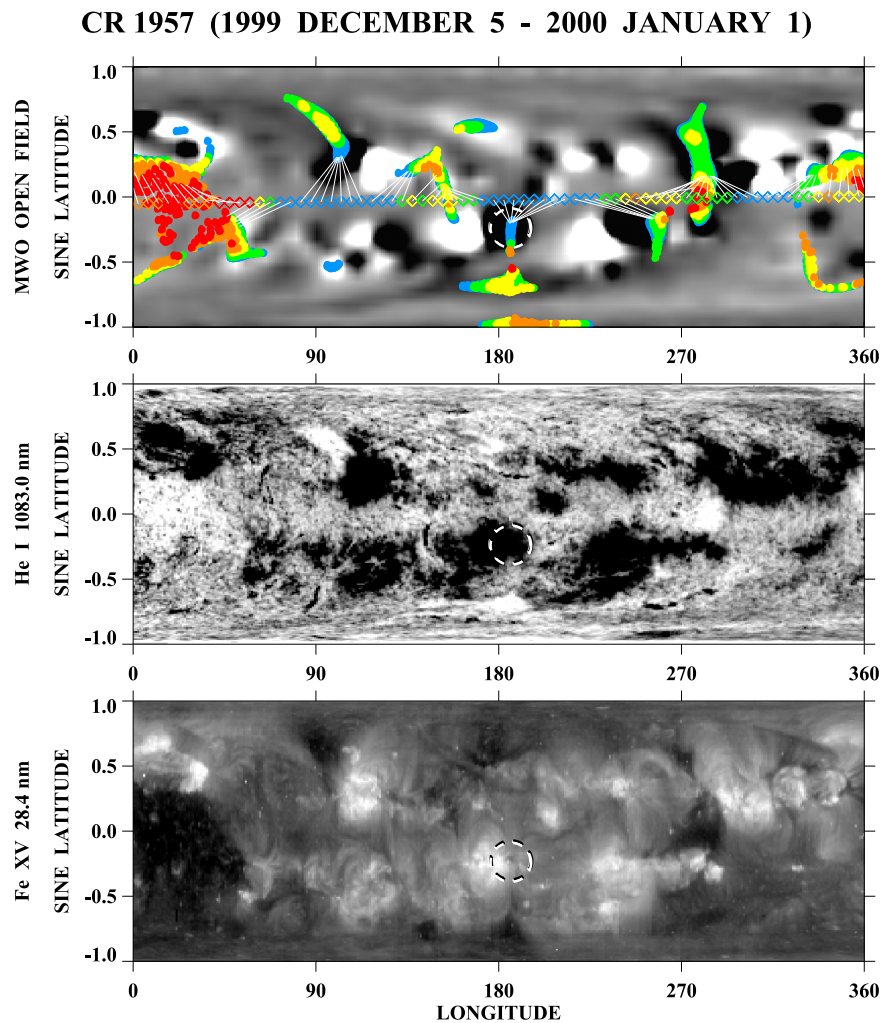
Figure 8. Carrington-format maps showing the predicted and observed configuration of coronal holes during CR 1957. Top panel: MWO photospheric field and PFSS-derived open-field regions. Grayscale and color contours are as in Figure 1. Middle panel: NSO map of He I 1083.0 nm intensity. Bottom panel: distribution of Fe XV 28.4 nm emission recorded by EIT. The circle at $\phi \sim 185°$ contains a dark 28.4 nm feature discussed in the text (see also Figure 9).

see Figure 9 of Liewer et al. 2004) gave $V \sim 400\text{--}550$ km s^{-1} and $O^{7+}/O^{6+} \sim 0.05\text{--}0.3$.

Liewer et al. (2004) reached very different conclusions about the nature of the solar-wind source. First, the open flux derived from their PFSS extrapolation of the NSO photospheric field was confined to the edge of AR 8681 rather than extending down to the equator, as indicated by our extrapolations of MWO, NSO, and WSO magnetograph measurements. The reason for this difference is unclear to us, although it provides another indication of the uncertainties involved in the coronal models. Second, their identification of coronal holes was based on the hand-drawn synoptic maps of He I 1083.0 nm hole boundaries provided by NSO, and the map for CR 1953 omits the near-equatorial hole that is unmistakably present in the original data. As a result, Liewer et al. (2004) inferred that the wind originated from a strong-field region associated with AR 8681 but lying outside the "large dark corridor" separating the two hemispheres in Fe XV 28.4 nm.

Returning to Figure 5, we note that the background unipolar region and its associated hole were present well before the emergence of AR 8681. Figure 6 shows a corresponding set of images taken on August 26. The dark area in Fe XV 28.4 nm now extends farther toward the northeast, into what appears to be the positive-polarity remnant of a recently decayed AR. A corresponding gap is seen in the strong He I 1083.0 nm absorption occurring in the plage region; this inlet is somewhat smaller than its 28.4 nm counterpart (compare the circled areas in Figure 6). Although the nature of this blurry, grayish feature is not obvious from the 1083.0 nm spectroheliogram alone, the 28.4 nm image (as well as the strongly unipolar background) suggests that it is almost certainly part of a coronal hole.

As illustrated in Figure 7, the emergence of AR 8681 into the plage region of Figure 6 led to the disappearance of the embedded hole. Here, in order to bring out the loop structures, we display a sequence of EIT Fe IX 17.1 nm images recorded during August 27–29, along with the corresponding MDI magnetograms. As negative, trailing-polarity flux (in the form of sunspot pores) emerges near the southern edge of the positive-polarity hole, loop connections progressively form to the interior of the hole, which fills up with bright material.

1999 DECEMBER 16 - 18

Fe XV 28.4 nm   MDI (100/-100 G)
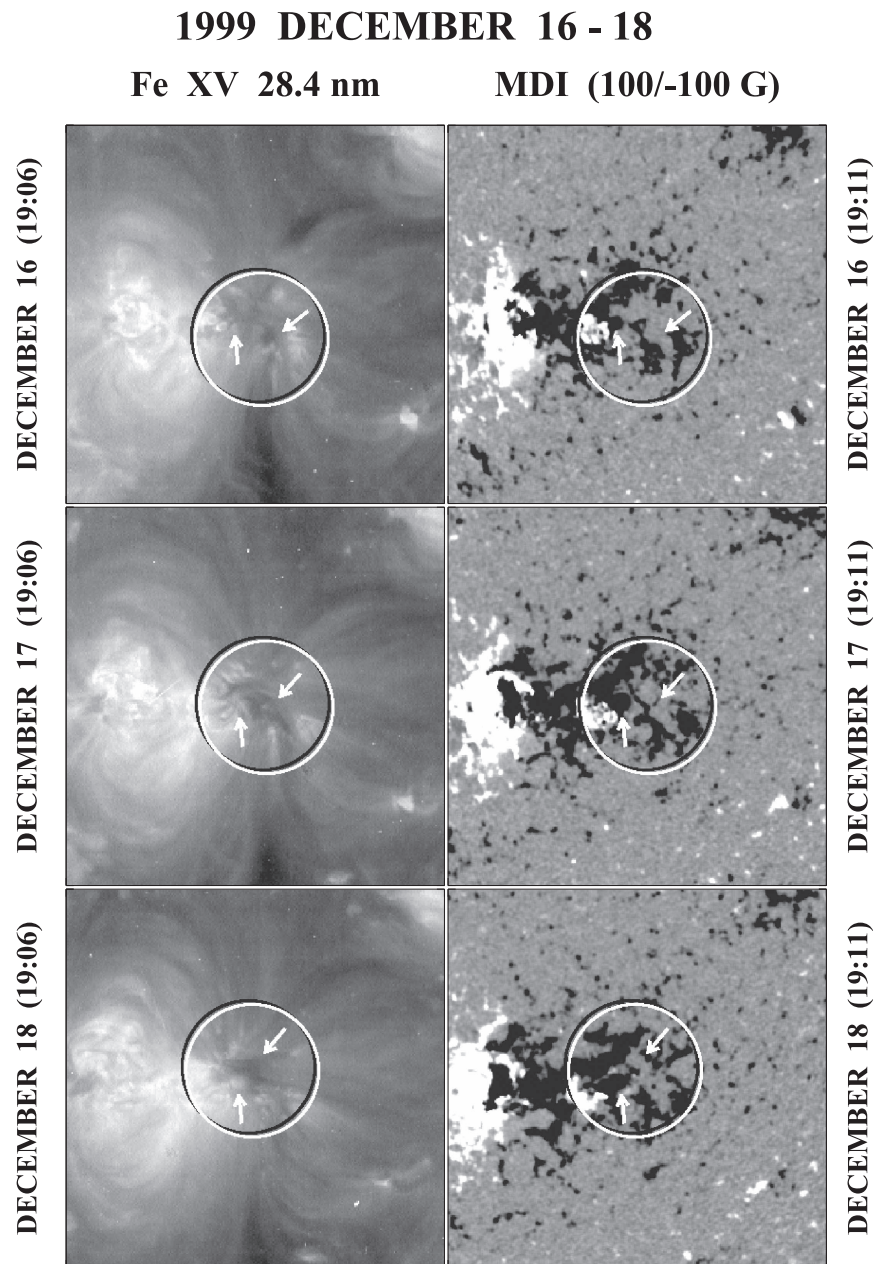
Figure 9. Evolution of the dark Fe XV 28.4 nm feature at the western edge of AR 8798 during 1999 December 16–18, as the AR rotates toward central meridian (left column). The right column displays the line-of-sight photospheric field, saturated at ±100 G. Circles have radius $113''$. The feature (indicated by an arrow) appears to grow as a negative-polarity sunspot (also arrowed) emerges just to its east. In the 28.4 nm image taken on December 16, a background coronal hole may be seen to the northwest of the circled area; this small, negative-polarity hole (not to be confused with the dark filament channel to its west) becomes less visible in the subsequent images.

3.3. Evidence for a Small Coronal Hole Inside AR 8798

We now consider the origin of the solar wind associated with AR 8798, which crossed central meridian on 1999 December 19, in the middle of CR 1957. The latitude–longitude maps of Figure 8 display the MWO photospheric field with the PFSS-derived open-field regions overplotted, the distribution of He I 1083.0 nm intensity from NSO, and the distribution of Fe XV 28.4 nm emission from EIT.

AR 8798 is centered near longitude $\phi \sim 175°$ and latitude $L \sim -13°$. As indicated by the circled area in the top panel of Figure 8, a narrow corridor of open flux bisects the negative-polarity, leading/western sector of the AR. The

equatorward edge of this corridor is magnetically connected to the ecliptic plane and is characterized by very rapid flux-tube expansion (blue denotes $f_{ss} > 35$). The corresponding wind speeds and charge-state ratios measured at ACE were $V \sim 300$–400 km s^{-1} and $O^{7+}/O^{6+} \sim 0.1$–0.4.

As shown by the middle panel of Figure 8, the corridor of open flux has no coronal hole signature in He I 1083.0 nm, but lies inside the dark area occupied by the AR. On the other hand, the Fe XV 28.4 nm map shows a small, dark feature located within the predicted open-flux region. This structure is not visible in the *Yohkoh* soft X-ray image used by Liewer et al. (2004; see their Figure 11), nor is it seen in EIT Fe XII 19.5 nm
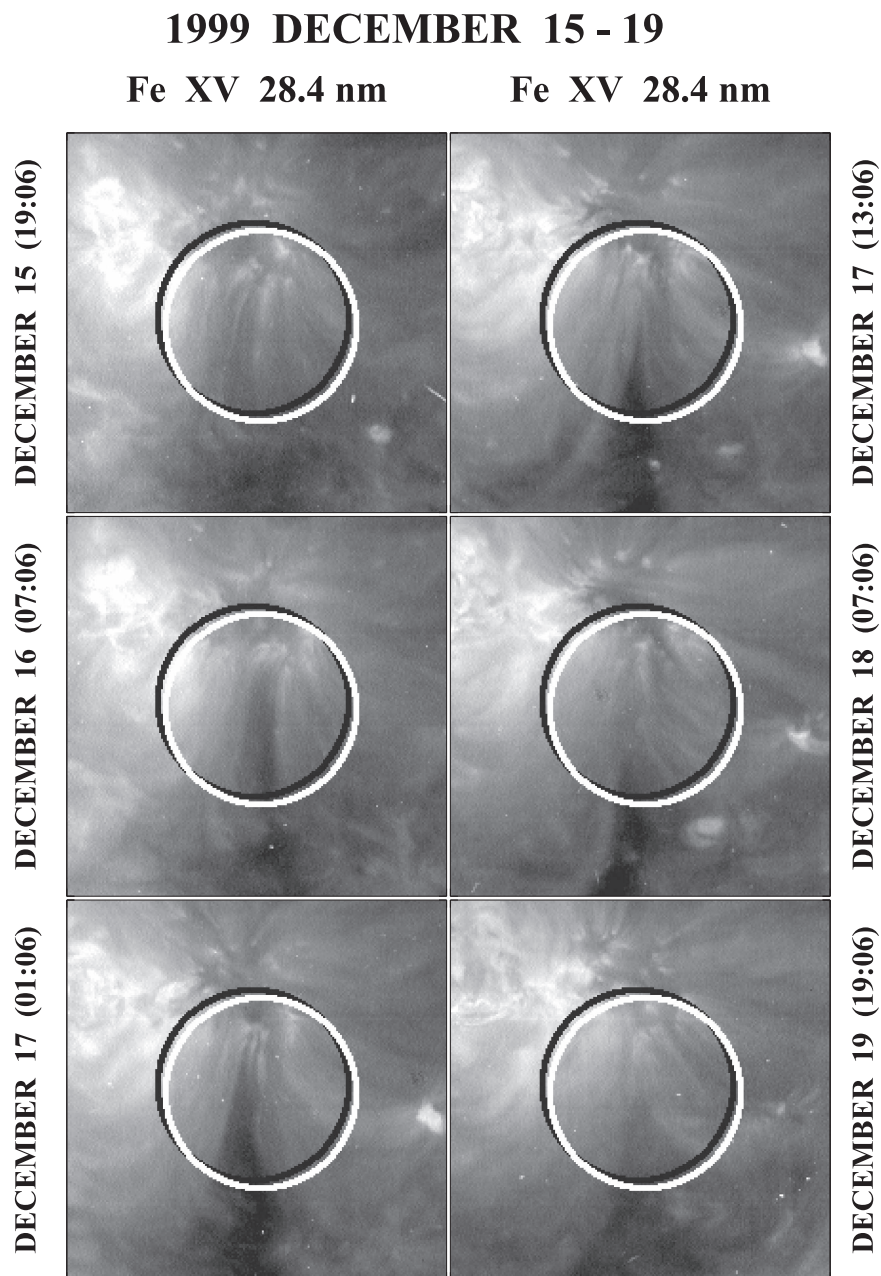
1999 DECEMBER 15 – 19

Figure 10. Sequence of Fe XV 28.4 nm images recorded during 1999 December 15–19, showing the dark corridor on the southwest side of AR 8798 and the effect of the overlying loops on its visibility as it rotates toward central meridian. Circles have radius 130″. The narrow corridor is predicted by the PFSS extrapolation of Figure 8, but does not appear in the 28.4 nm synoptic map, which was constructed from central meridian data.

images, where it may be obscured by the overlying loop structures.

Figure 9 shows the evolution of the 28.4 nm feature during December 16–18, together with the corresponding MDI magnetograms. The feature first becomes visible on December 16, as a dark dot located just westward of an area of emerging flux within the negative-polarity sector of AR 8798. The emerging BMR contains a negative-polarity sunspot, which grows over the next two days. At the same time, the adjacent 28.4 nm feature appears to expand in the northeast and southwest directions, to encompass a few supergranular cells. Although projection effects may have contributed to the changes in the size and shape of the dark structure, the opening-up of flux and the growth of a small coronal hole are consistent with the observed

strengthening of the negative-polarity background by the emerging sunspot.

The dark feature tracked in Figure 9 is situated at the equatorward end of the corridor of negative-polarity open flux predicted by the PFSS extrapolation (top panel of Figure 8). Inspection of the 28.4 nm image taken on December 16 (top left panel of Figure 9) suggests the presence of a dark lane that terminates just southward of the highlighted feature, but which is no longer detectable in the subsequent images. As illustrated by the sequence of 28.4 nm images in Figure 10, the dark channel reaches its maximum visibility on December 16–17. Both before and after this time, it is covered by the long loops rooted at its northern end. For this reason, the corridor does not appear in

CR 2146 (2014 JANUARY 15 - FEBRUARY 11)
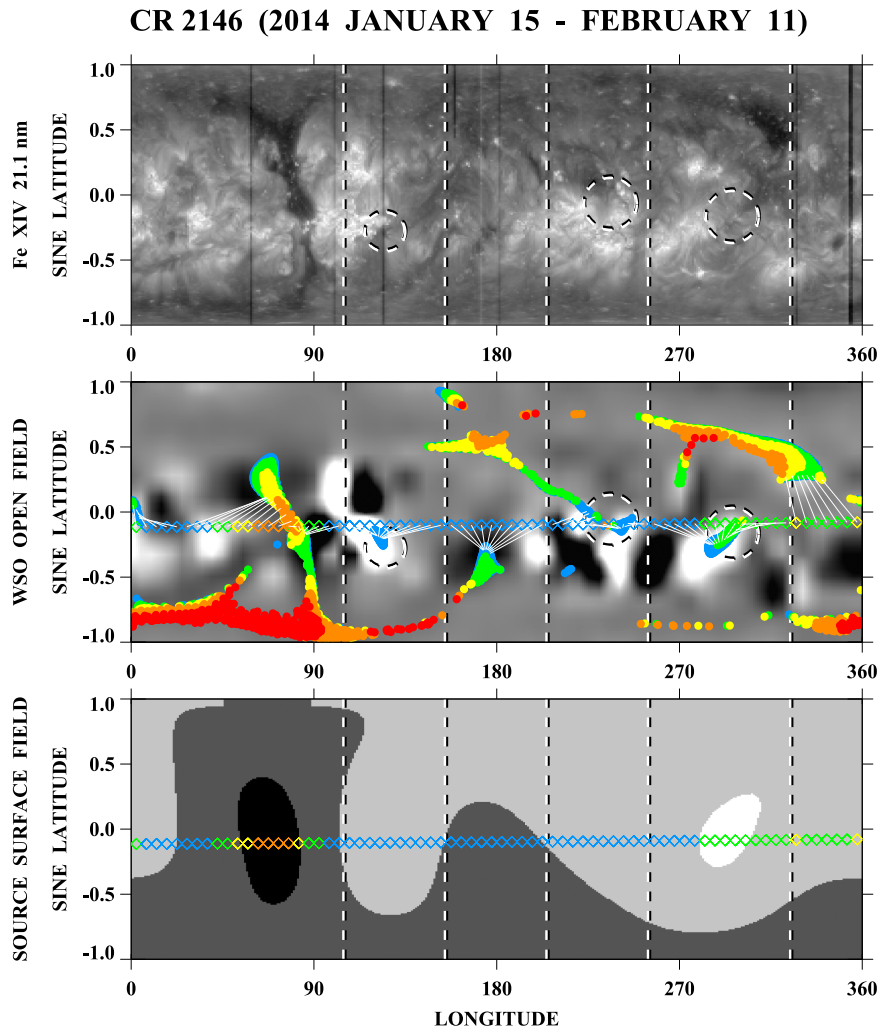
Figure 11. Carrington-format maps showing the observed and PFSS-predicted configuration of coronal holes and the source-surface field during CR 2146. Top panel: distribution of Fe XIV 21.1 nm emission recorded by *SDO*/AIA. Middle panel: WSO photospheric field (saturated at $B_r = \pm 20$ G) with PFSS-derived open-field regions overplotted as colored dots. Colored diamonds (plotted in the ecliptic plane) indicate the expansion factors of Earth-directed flux tubes, with white lines connecting them to their footpoint areas. Color-coding for dots and diamonds is as in previous figures: blue ($f_{ss} > 35$), green ($15 < f_{ss} < 35$), yellow ($8 < f_{ss} < 15$), orange ($4 < f_{ss} < 8$), and red ($f_{ss} < 4$). Bottom panel: source-surface field $B_{ss} \equiv B_r(R_{ss}, L, \phi)$. Black: $B_{ss} < -0.15$ G. Dark gray: -0.15 G $< B_{ss} < 0$ G. Light gray: 0 G $< B_{ss} < +0.15$ G. White: $B_{ss} > +0.15$ G. Colored diamonds again indicate the expansion factors of Earth-directed flux tubes. Source regions discussed in the text are circled, with vertical dashed lines indicating the predicted longitudinal ranges of their in-ecliptic wind streams.

the 28.4 nm synoptic map in the bottom panel of Figure 8. The changing visibility of this narrow feature appears to be a consequence of both intrinsic variations in the overlying loop structure and changes in the viewing angle.

3.4. Masking of AR-associated Coronal Holes in He I 1083.0 nm

It is generally accepted that illumination by coronal radiation from above plays a major role in the formation of the He I 1083.0 nm line (see, e.g., Avrett et al. 1994; Andretta & Jones 1997). The EUV flux shortward of 50.4 nm photoionizes the neutral helium atoms near the top of the chromosphere, which recombine to populate the metastable lower level of the line, leading to the absorption of continuum radiation from the photosphere. An additional contribution may come from the lower transition region, where the temperatures are sufficiently high to populate the lower level by direct collisional excitation. The amount of absorption depends on the intensity of the

coronal radiation and on the density/temperature stratification. The dark appearance of ARs in He I 1083.0 nm spectroheliograms is attributed to the strength of the EUV flux impinging on the chromosphere, while the smooth, white appearance of coronal holes outside ARs is due to the weakness of the EUV flux from above.

Consider now the case of a small area of open flux that forms inside or next to an AR or within a strong plage region (as in Figure 6). Because the coronal plasma continually escapes along the field lines but cannot cross them, the open-field region will have lower electron densities n_e than the surrounding corona; in the absence of projection effects, it will therefore appear as a "hole" in the coronal EUV emission, which scales as n_e^2. Because photons are not tied to the magnetic field, however, the chromospheric footpoints of the EUV hole will be bombarded by radiation from the neighboring bright coronal loops, so that these footpoint areas will be grayish or even dark in He I 1083.0 nm

CR 2146 (2014 JANUARY 15 - FEBRUARY 11)
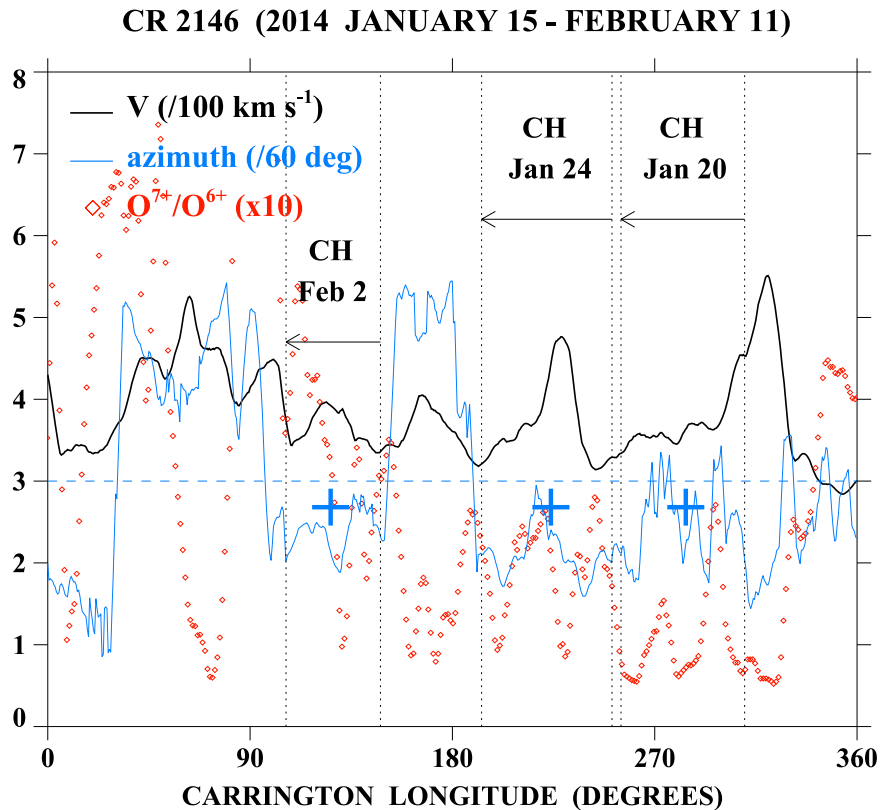
Figure 12. Variation of the solar-wind speed and O^{7+}/O^{6+} ratio during CR 2146, plotted as a function of Carrington longitude to facilitate comparison with Figure 11. Also plotted is the IMF azimuth angle, measured counterclockwise from the Sun–Earth line and lying in the quadrant $90°–180°$ ($270°–360°$) if the IMF points away from (toward) the Sun. (Horizontal dashed line indicates an azimuth angle of $180°$.) The OMNI and *ACE*/SWICS measurements have been smoothed by taking 10 hr running means, and have been mapped back to the source surface assuming a four-day Sun–Earth propagation time. Values of $O^{7+}/O^{6+} \lesssim 0.1$ are uncertain by factors of ~ 2. Wind streams associated with the circled areas in Figure 11 are marked by arrows and vertical dotted lines, and labeled with the date of central meridian passage of the source region.

spectroheliograms. Thus, in Figure 6, the 1083.0 nm counterpart of the EUV hole appears darkest where the adjacent Fe XV 28.4 nm emission is brightest; in the case of the small hole circled in the 28.4 nm map of Figure 8 (see also Figure 9), the corresponding area in the 1083.0 nm map is as dark as the surrounding AR.

These considerations suggest that the identification of coronal holes should not be based solely on He I 1083.0 nm spectroheliograms, but should exploit all of the available data, including EUV and soft X-ray observations, which provide a more direct measure of the coronal density. In particular, small coronal holes located in and around ARs may be invisible in He I 1083.0 nm but detectable in EUV images, although the converse may sometimes hold due to project effects (as indicated by Figure 1, near $\phi = 215°$). It should also be recognized that, because the overlying loop structure and the diffuse foreground emission vary from one EUV channel to another, a coronal hole may sometimes be detectable in one EUV emission line but not another.

4. AR-associated Coronal Holes During the 2014 Sunspot Maximum

When the current solar cycle reached its peak in early 2014, low-speed solar wind predominated in the ecliptic plane. As we now show using PFSS extrapolations and EUV observations

from *SDO*, a major contribution to this slow wind came from small coronal holes near ARs.

4.1. Small Coronal Holes and Dark Corridors During CR 2146

Figure 11 (top panel) displays a map of Fe XIV 21.1 nm intensity constructed from individual *SDO* images taken during CR 2146 (2014 January 15–February 11). The middle panel shows the WSO photospheric field with PFSS-derived open-field regions (color-coded as in previous figures) superposed, while the bottom panel shows the corresponding source-surface field; colored diamonds again indicate the expansion factors of Earth-directed flux tubes. The circled areas highlight some of the small EUV holes whose open-field counterparts are connected to the ecliptic plane.

In Figure 12, the wind speeds and O^{7+}/O^{6+} ratios recorded at *ACE* during CR 2146 are plotted as a function of Carrington longitude ϕ; time runs from right to left and a four-day shift has been applied to account roughly for the Sun–Earth propagation time. Also plotted is the IMF azimuth angle, defined such that relatively high (low) values indicate $B_r < 0$ ($B_r > 0$). The wind streams corresponding to the circled areas in Figure 11 are marked off by vertical dotted lines and labeled with the central meridian passage dates of their source regions.

Consider first the circled area near $\phi \sim 295°$ in Figure 11, which contains some very small, darkish 21.1 nm features that lie within the predicted open-field region in the middle
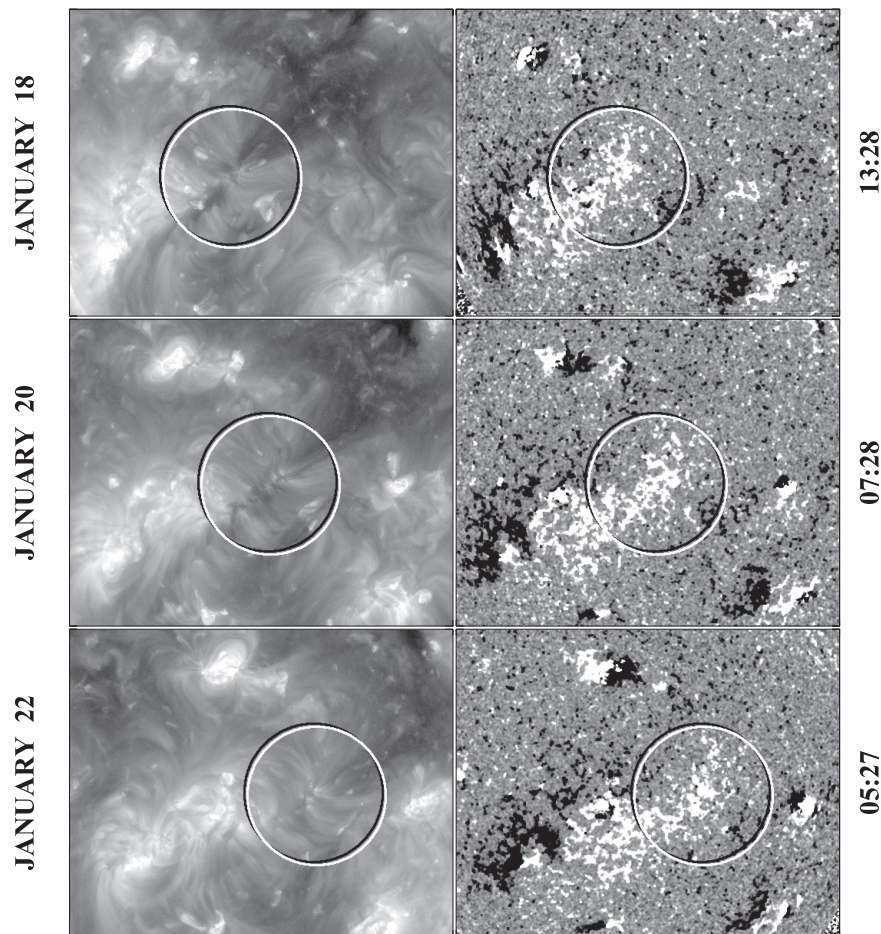
Figure 13. Close-up views of the dark channel located at longitude ∼295° in Figure 11, as it appeared before, during, and after its central meridian passage. Left column: Fe XIV 21.1 nm images recorded by *SDO* on 2014 January 18, 20, and 22. Right column: corresponding HMI line-of-sight magnetograms, saturated at ±20 G. Circles have radius 216″. The elongated coronal hole is clearly visible when it lies east of the central meridian, but becomes progressively narrower as it rotates westward, mainly due to projection effects associated with the nonradial orientation of the surrounding loops.

panel. The PFSS extrapolation suggests that this narrow, fragmented structure is the source of the slow ($V \sim 350\,\mathrm{km\,s^{-1}}$) wind observed by *ACE* in the longitude range ∼260°–300° (Figure 12). At its northwest end, the corridor widens and darkens to resemble a "normal" coronal hole, which may account for the steep increase in the wind speed near $\phi \sim 300°$.

The Fe XIV 21.1 nm images in Figure 13 focus on the corridor as it rotated across the disk during January 18–22. The structure appears at its darkest and widest on January 18, when it lies to the east of central meridian. Comparing the 21.1 nm image with the simultaneous HMI magnetogram in the right column of Figure 13, we see that the channel is embedded within the sheared, positive-polarity sector of a decaying AR, with a negative-polarity region located on either side. As described by Švestka et al. (1977), this type of quadrupolar configuration gives rise to a lane of open flux separating the core of the AR from the neighboring region, which is observed as a dark X-ray/EUV corridor.

At central meridian passage on January 20, the 21.1 nm corridor seems to have become even narrower (see the middle left panel of Figure 13); it is thus barely visible in the synoptic map of Figure 11, which was assembled from central meridian observations. By January 22, only the overlying coronal loops are evident in the 21.1 nm image. Since the magnetograms show no major changes in the ambient photospheric field during this four-day period, we attribute the progressive narrowing of the dark channel to projection effects and in particular to changes in the angle between the line of sight and the nonradially oriented loops surrounding the channel.

The probable source of the wind stream at longitudes ∼200°–240° (Figure 12) is the dark EUV hole at $\phi \sim 230°$ in Figure 11, straddling the northeastern boundary of the circled area. Toward the western edge of the circle, we also see a dark lane resembling that at $\phi \sim 295°$. As illustrated by Figure 14, this feature (which crossed central meridian early on January 24) became progressively more visible as it rotated from east to west during

2014 JANUARY 21 - 25

21.1 nm   HMI (20/-20 G)
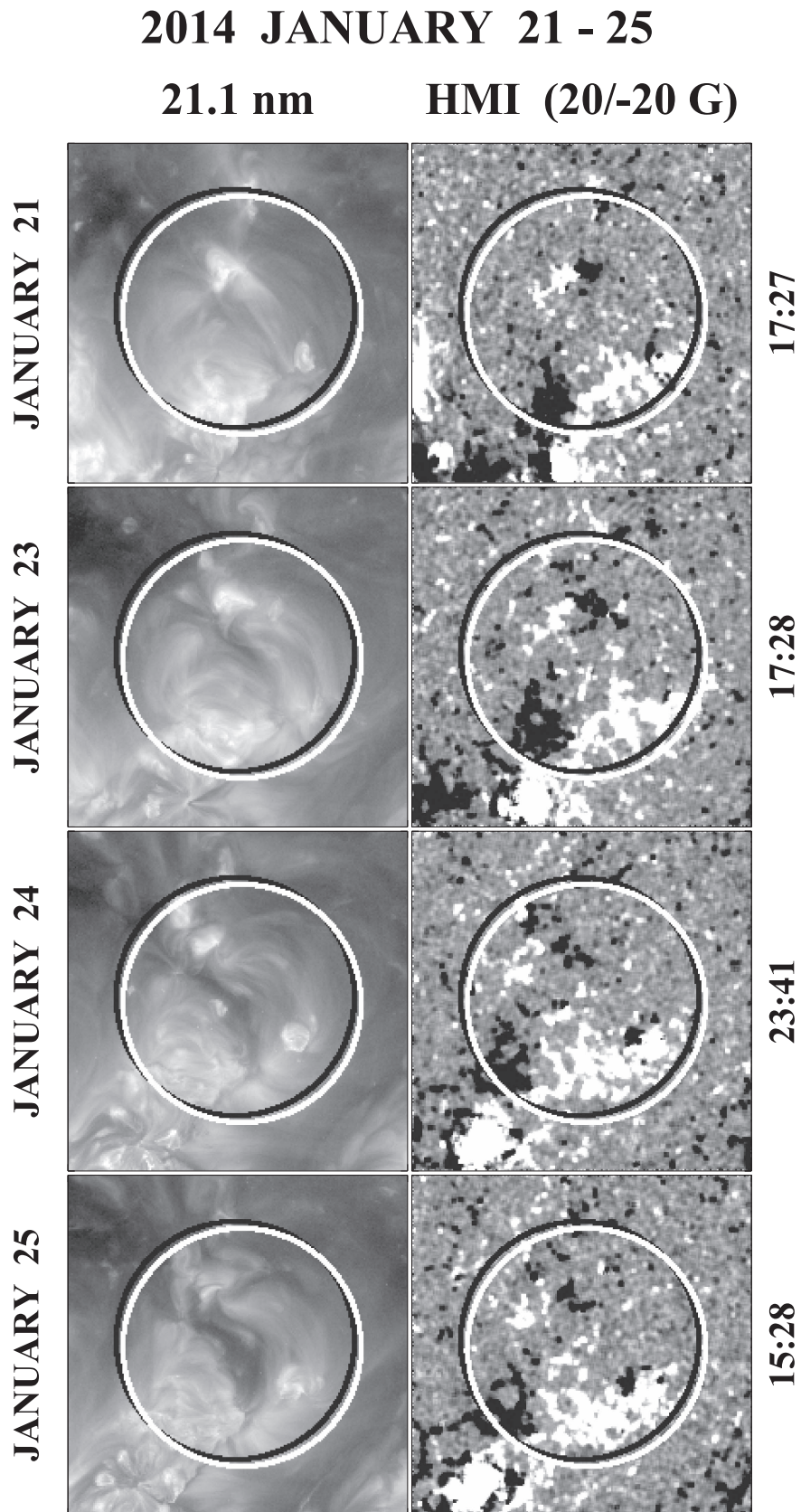
Figure 14. Successive views of the dark lane at $\phi \sim 240°-245°$ in Figure 11, as it appeared before and after its central meridian passage early on January 24. Left column: Fe XIV 21.1 nm images recorded on January 21, 23, 24, and 25. Right column: corresponding magnetograms, saturated at ± 20 G. Circles have radius 168″. In this case, the dark structure is initially hidden behind the loop system along its western boundary, but becomes increasingly visible as the region rotates westward.

## 2014 FEBRUARY 1 - 3

February 1 (17:28)   February 3 (03:28)
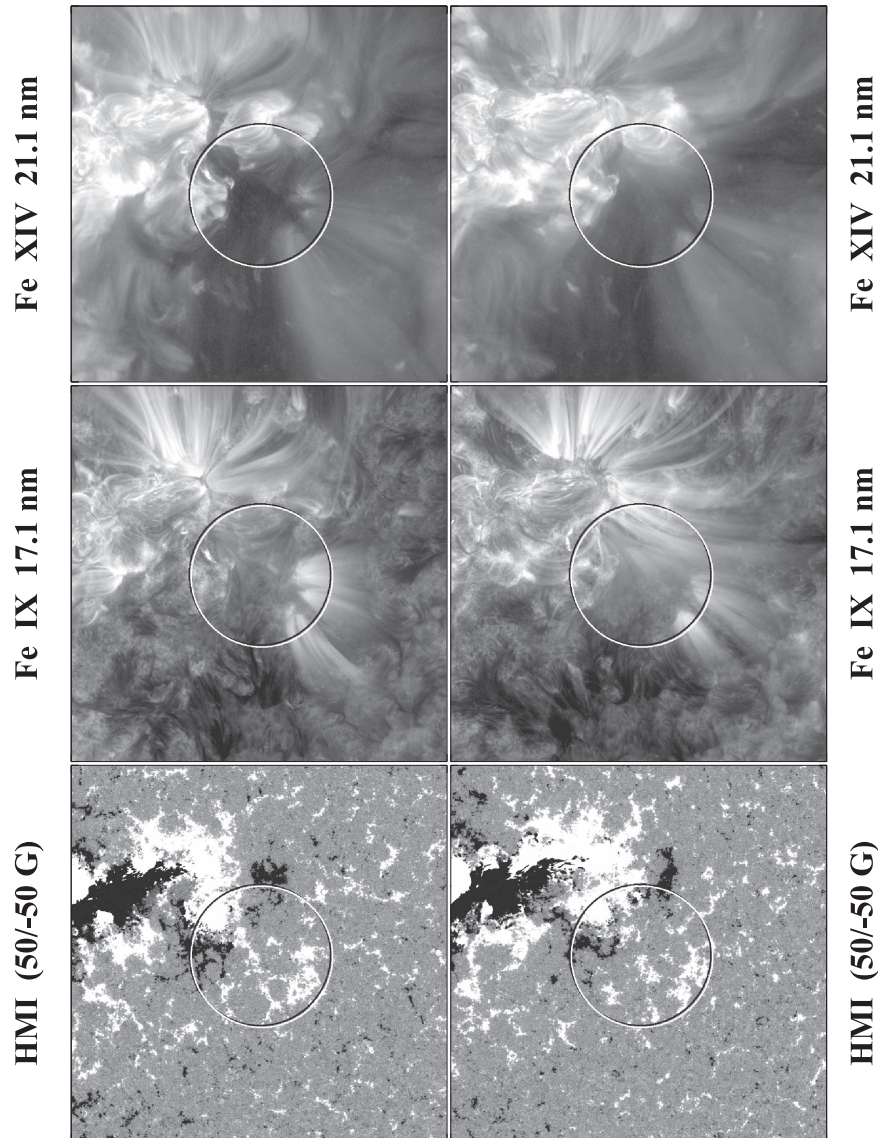
Figure 15. Close-up views of the dark structure at $\phi \sim 125°$ in Figure 11, as it appeared just before and just after central meridian passage on 2014 February 2. Left column: Fe XIV 21.1 nm and Fe IX 17.1 nm images and a magnetogram recorded at 17:28 UTC on February 1. Right column: corresponding set of images recorded at 03:28 UTC on February 3. HMI magnetograms are saturated at ± 50 G, and circles have radius $90''$. In the 21.1 nm image taken on February 1, the dark area extends into the positive-polarity sunspot and beyond; note also the narrow lane curving around the southern edge of the activity complex. The increase in the overlying diffuse emission on February 3 is at least partly a result of the emerging sunspot fields to the north of the circled area.

January 21–25. The increase in visibility may be related to the presence of the loop arcade on the west side of the narrow hole, which intercepts the observer's view when the hole lies eastward of disk center.

The circle at $\phi \sim 125°$ encloses a small, dark EUV feature located within a predicted area of open flux; the corresponding in situ measurements indicate wind speeds of order 350 km s^{-1} and highly variable O^{7+}/O^{6+} in the range ~ 0.1–0.5. Figure 15 presents close-up views of the source region just before and after central meridian passage, as seen in Fe XIV 21.1 nm, Fe IX 17.1 nm, and the corresponding HMI magnetograms. The 21.1 nm image recorded on February 1 shows a coronal hole centered just to the

southwest of a positive-polarity sunspot. An appendage of the dark region extends through the sunspot itself and continues northward, in the form of a narrow channel, into the plage region beyond. (Evidence for open flux extending into sunspots has been presented earlier by Schrijver & DeRosa 2003.) A dark lane may also be seen curving southeastward from the main body of the coronal hole and running along the southern edge of the activity complex, where it separates the loops linked to the AR from those linked to the negative-polarity background region in the south. On February 3, the entire dark area shows less contrast with the background corona. As suggested by the 17.1 nm image, the increase in the overlying coronal

CR 2148 (2014 MARCH 11 - APRIL 7)
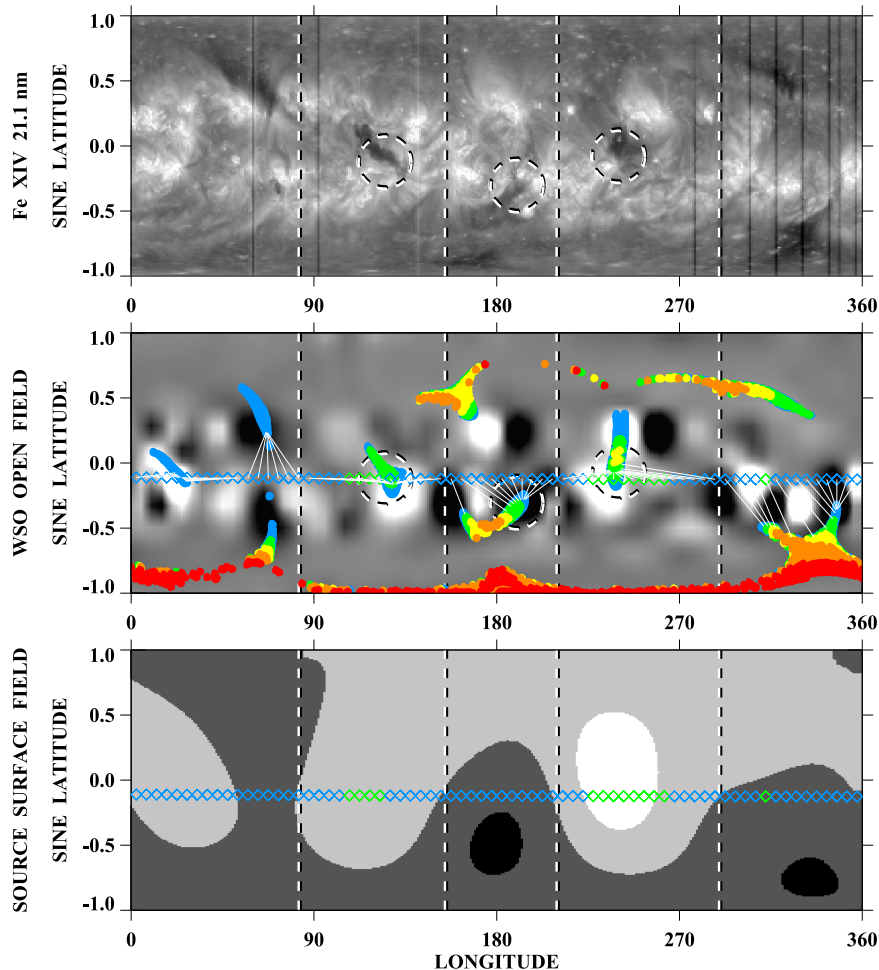
Figure 16. Carrington-format maps showing the observed and PFSS-predicted configuration of coronal holes and the source-surface field during CR 2148. Top panel: distribution of Fe XIV 21.1 nm emission recorded by *SDO*/AIA. Middle panel: WSO photospheric field (saturated at $B_r = \pm20$ G) with open-field regions overplotted as colored dots. Bottom panel: source-surface field. Grayscale and color-coding are as in Figure 11. Circles enclose some of the EUV coronal holes that produced moderately slow wind at Earth (see Figure 17).

emission is probably caused by changes in the surrounding loop structure due to the emerging sunspot fields just northeastward of the circled area.

4.2. AR-associated Coronal Holes and Slow Wind During CR 2148

Figure 16 shows the distribution of Fe XIV 21.1 nm emission, the WSO photospheric field with derived open-field regions, and the source-surface field for CR 2148 (2014 March 11–April 7). The wind speeds and oxygen charge-state ratios measured at *ACE* during this period are plotted against Carrington longitude in Figure 17.

From Figure 17, we see that the entire 27 day period was dominated by solar wind with speeds on the order of 400 km s^{-1} and O^{7+}/O^{6+} ratios of ~0.05–0.4 (ignoring the large spikes associated with transient events); as usual, the charge-state ratios tend to rise steeply near sector boundaries. The circled areas in Figure 16 indicate three of the low-latitude sources of this relatively slow wind. That the source regions are dark, clearly defined EUV holes of modest size provides further confirmation that coronal holes may

give rise to a wide range of wind speeds. The Earth-directed flux tubes of the corresponding open-field regions are characterized by large expansion factors (coded blue and green). A comparison between individual 21.1 nm images and HMI magnetograms shows that the EUV holes are located not within the recently emerged ARs, but inside the adjacent unipolar regions that contain weaker fields (~30 G) left over from earlier ARs. As is generally the case for coronal holes that straddle the equator, the equatorial holes at longitudes ~125° and ~240° are embedded inside flux that has diffused equatorward from the AR zones in both hemispheres.

5. Summary and Discussion

Our main points may be summarized as follows:

1. The visual identification of coronal holes, defined as regions of reduced coronal density that are magnetically connected to the interplanetary medium, should be based on all of the available imaging data, and not rely on any single wavelength channel. In particular, although sometimes adopted as the "gold standard," He I 1083.0 nm
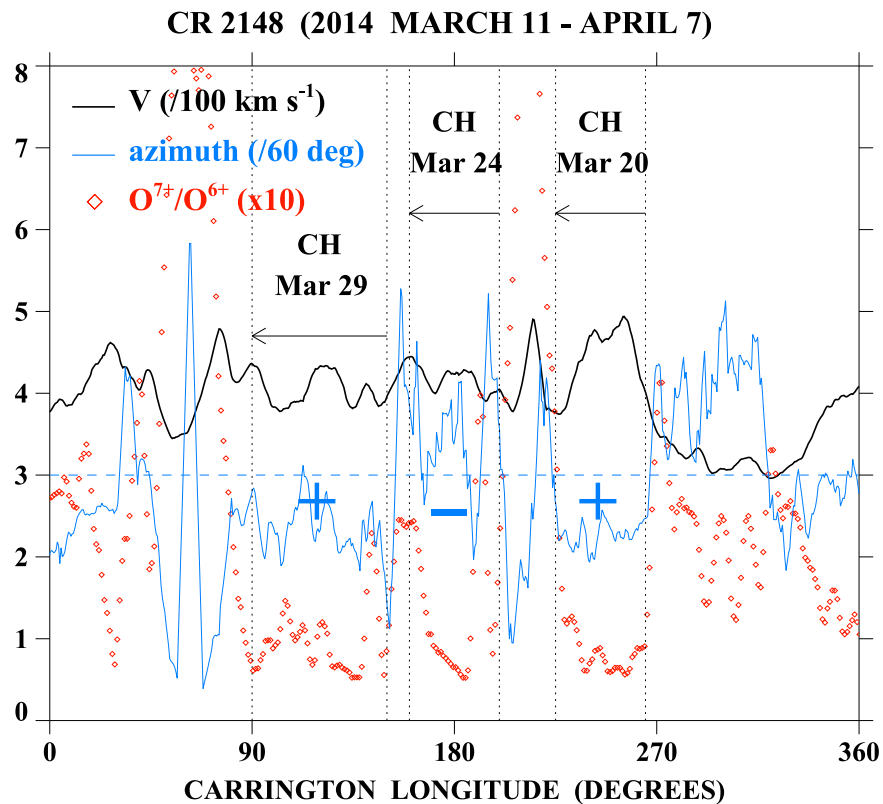
Figure 17. Variation of the solar wind speed, O^{7+}/O^{6+} ratio, and IMF azimuth angle during CR 2148, plotted as a function of Carrington longitude after applying a four-day shift (see also Figure 12 caption). Wind streams associated with the circled EUV holes in Figure 16 are marked by arrows and vertical dotted lines, and labeled with the date of the central meridian passage of the hole.

does not provide a direct measure of coronal density, and small holes near ARs may appear in absorption if the photoionizing flux from the neighboring coronal loops is sufficiently large. On the other hand, as illustrated by Figure 1 (near longitude 215°), some holes may be visible in 1083.0 nm while being obscured by the overlying diffuse emission in EUV images.

2. Because the magnetic field tends to fan out nonradially from the edges of ARs, the underlying EUV holes are sometimes more visible toward one solar limb than at central meridian (see Figures 10, 13, and 14). Such holes may be overlooked in synoptic maps.

3. AR-associated EUV coronal holes are usually embedded inside unipolar areas located at the peripheries of ARs, not inside the ARs themselves. These background regions contain moderately strong ($\sim 30\,\mathrm{G}$) fields that are the remnants of recently decayed ARs.

4. However, EUV holes sometimes extend into the cores of ARs, and even into sunspots (Figure 15; see also Schrijver & DeRosa 2003). This penetration of open flux into an AR may occur if the two polarities are sufficiently unbalanced, as when a BMR emerges within a strong unipolar region.

5. At sunspot maximum, unipolar regions tend to be relatively narrow because the ARs from which they originate are closely spaced in longitude; the embedded coronal holes are thus often elongated in the direction of the nearby photospheric neutral lines and may appear as

narrow corridors (as in Figure 13; see also Švestka et al. 1977).

6. Small holes in and around ARs tend to evolve rapidly, with their boundaries changing in response to nearby flux emergence (see, e.g., Figure 7) and to transient activity such as flares and filament eruptions.

7. Small AR-associated coronal holes are a major source of the slow wind prevalent at sunspot maximum. As at other phases of the solar cycle, low-speed wind also comes from the rapidly diverging flux tubes rooted near the boundaries of all coronal holes, regardless of their size or location; this component of the slow wind is concentrated around the heliospheric current sheet (or IMF sector boundaries).

The solar cycle evolution of coronal holes (regarded as the observational manifestations of open-field regions) closely reflects the evolution of unipolar regions, which have their sources in ARs (large BMRs). Each polarity sector of a BMR represents an embryo unipolar region, which grows in areal size as transport processes (supergranular convection/diffusion, differential rotation, and poleward meridional flow) act to spread the flux and weaken the field. Near sunspot maximum, the growth of unipolar regions at low latitudes is continually disrupted by new flux emergence, so that the embedded coronal holes tend to be small and short-lived. (This limitation does not apply to the polar fields and polar holes, which continue to grow as meridional flow transports net trailing-polarity flux from the sunspot latitudes to the poles.)

As sunspot activity declines, the unipolar regions merge to form much larger structures, which may persist for months to years before all of the remaining unbalanced flux is annihilated by surface transport processes. The coronal holes embedded in these weak remnant fields are correspondingly large and long-lived, and are the sources of the recurrent high-speed streams that dominate the declining phase of the cycle. Although they often appear to be unrelated to ARs, these extended areas of open flux, interspersed with smaller-scale, closed-loop systems, owe their existence to the flux injected by many earlier ARs. In that sense, all coronal holes have their origin in ARs; small bipoles and ephemeral regions, while continually "churning" the field on short timescales, cannot give rise to large-scale unipolar areas. The basic physical properties that distinguish the small holes observed at solar maximum from their larger successors during the declining phase are their much stronger footpoint fields, greater rates of flux-tube divergence, and more rapid evolution.

References

Abbo, L., Ofman, L., Antiochos, S. K., et al. 2016, SSRv, 201, 55
Andretta, V., & Jones, H. P. 1997, ApJ, 489, 375
Arge, C. N., & Pizzo, V. J. 2000, JGR, 105, 10465
Avrett, E. H., Fontenla, J. M., & Loeser, R. 1994, in Proc. IAU Symp. 154, Infrared Solar Physics, ed. D. M. Rabin, J. T. Jefferies, & C. Lindsey (Dordrecht: Kluwer), 35
Brooks, D. H., Ugarte-Urra, I., & Warren, H. P. 2015, NatCo, 6, 5947
Cohen, O. 2015, SoPh, 290, 2245
Cranmer, S. R., van Ballegooijen, A. A., & Edgar, R. J. 2007, ApJS, 171, 520
Fazakerley, A. N., Harra, L. K., & van Driel-Gesztelyi, L. 2016, ApJ, 823, 145
Fu, H., Li, B., Li, X., et al. 2015, SoPh, 290, 1399
Fu, H., Madjarska, M. S., Xia, L., et al. 2017, ApJ, 836, 169
Fujiki, K., Tokumaru, M., Hayashi, K., Satonaka, D., & Hakamada, K. 2016, ApJL, 827, L41
Ko, Y.-K., Muglach, K., Wang, Y.-M., Young, P. R., & Lepri, S. T. 2014, ApJ, 787, 121
Levine, R. H. 1982, SoPh, 79, 203
Levine, R. H., Altschuler, M. D., & Harvey, J. W. 1977, JGR, 82, 1061
Liewer, P. C., Neugebauer, M., & Zurbuchen, T. 2003, in AIP Conf. Proc. 679, Solar Wind Ten, ed. M. Velli, R. Bruno, & F. Malara (Melville, NY: AIP), 51
Liewer, P. C., Neugebauer, M., & Zurbuchen, T. 2004, SoPh, 223, 209
Luhmann, J. G., Li, Y., Arge, C. N., Gazis, P. R., & Ulrich, R. 2002, JGR, 107, 1154
Neugebauer, M., Forsyth, R. J., Galvin, A. B., et al. 1998, JGR, 103, 14587
Neugebauer, M., Liewer, P. C., Smith, E. J., Skoug, R. M., & Zurbuchen, T. H. 2002, JGR, 107, 1488
Poduval, B. 2016, ApJL, 827, L6
Riley, P., Linker, J. A., Mikić, Z., et al. 2006, ApJ, 653, 1510
Schrijver, C. J., & DeRosa, M. L. 2003, SoPh, 212, 165
Schwadron, N. A., Fisk, L. A., & Zurbuchen, T. H. 1999, ApJ, 521, 859
Sheeley, N. R., Jr., Lee, D. D.-H., Casto, K. P., Wang, Y.-M., & Rich, N. B. 2009, ApJ, 694, 1471
Švestka, Z., Solodyna, C. V., Howard, R., & Levine, R. H. 1977, SoPh, 55, 359
Wang, Y.-M., Hawley, S. H., & Sheeley, N. R., Jr. 1996, Sci, 271, 464
Wang, Y.-M., Ko, Y.-K., & Grappin, R. 2009, ApJ, 691, 760
Wang, Y.-M., Robbrecht, E., Rouillard, A. P., Sheeley, N. R., Jr., & Thernisien, A. F. R. 2010, ApJ, 715, 39
Wang, Y.-M., & Sheeley, N. R., Jr. 1990, ApJ, 355, 726
Wang, Y.-M., & Sheeley, N. R., Jr. 1992, ApJ, 392, 310
Wang, Y.-M., & Sheeley, N. R., Jr. 1995, ApJL, 447, L143
Wang, Y.-M., & Sheeley, N. R., Jr. 2003, ApJ, 587, 818
Wang, Y.-M., & Sheeley, N. R., Jr. 2004, ApJ, 612, 1196
Wang, Y.-M., Sheeley, N. R., Jr., Socker, D. G., Howard, R. A., & Rich, N. B. 2000, JGR, 105, 25133
Zurbuchen, T. H., Hefti, S., Fisk, L. A., Gloeckler, G., & Schwadron, N. A. 2000, JGR, 105, 18327